Wildfire Smoke Observations in the Western United States from the Airborne Wyoming Cloud Lidar during the BB-FLUX Project. Part I: Data Description and Methodology

MIN DENG,[a,b] ZHIEN WANG,[b,c] RAINER VOLKAMER,[c,d,e] JEFFERSON R. SNIDER,[a] LARRY OOLMAN,[a] DAVID M. PLUMMER,[a] NATALIE KILLE,[c,e] KYLE J. ZARZANA,[d] CHRISTOPHER F. LEE,[d,e] TERESA CAMPOS,[f] NICHOLAS RYAN MAHON,[a] BRENT GLOVER,[a] MATTHEW D. BURKHART,[a] AND AUSTIN MORGAN[a]

[a] *Department of Atmospheric Science, University of Wyoming, Laramie, Wyoming*
[b] *Laboratory of Atmosphere and Space Physics, University of Colorado Boulder, Boulder, Colorado*
[c] *Department of Atmospheric and Oceanic Sciences, University of Colorado Boulder, Boulder, Colorado*
[d] *Department of Chemistry, University of Colorado Boulder, Boulder, Colorado*
[e] *Cooperative Institute for Research in Environmental Sciences, University of Colorado Boulder, Boulder, Colorado*
[f] *National Center for Atmospheric Research, Boulder, Colorado*

(Manuscript received 12 July 2021, in final form 13 December 2021)

ABSTRACT: During the summer of 2018, the upward-pointing Wyoming Cloud Lidar (WCL) was deployed on board the University of Wyoming King Air (UWKA) research aircraft for the Biomass Burning Flux Measurements of Trace Gases and Aerosols (BB-FLUX) field campaign. This paper describes the generation of calibrated attenuated backscatter coefficients and aerosol extinction coefficients from the WCL measurements. The retrieved aerosol extinction coefficients at the flight level strongly correlate (correlation coefficient, rr $>$ 0.8) with in situ aerosol concentration and carbon monoxide (CO) concentration, providing a first-order estimate for converting WCL extinction coefficients into vertically resolved CO and aerosol concentration within wildfire smoke plumes. The integrated CO column concentrations from the WCL data in nonextinguished profiles also correlate (rr = 0.7) with column measurements by the University of Colorado Airborne Solar Occultation Flux instrument, indicating the validity of WCL-derived extinction coefficients. During BB-FLUX, the UWKA sampled smoke plumes from more than 20 wildfires during 35 flights over the western United States. Seventy percent of flight time was spent below 3 km above ground level (AGL) altitude, although the UWKA ascended up to 6 km AGL to sample the top of some deep smoke plumes. The upward-pointing WCL observed a nearly equal amount of thin and dense smoke below 2 km and above 5 km due to the flight purpose of targeted fresh fire smoke. Between 2 and 5 km, where most of the wildfire smoke resided, the WCL observed slightly more thin smoke than dense smoke due to smoke spreading. Extinction coefficients in dense smoke were 2–10 times stronger, and dense smoke tended to have larger depolarization ratio, associated with irregular aerosol particles.

KEYWORDS: Aircraft observations; Algorithms; In situ atmospheric observations; Lidars/Lidar observations; Remote sensing; Biomass burning; Wildfires

1. Introduction

Wildfire in the western United States has a strong annual cycle, which maximizes around May–September, as the prolonged drought and extreme heat wave in the summer tend to trigger more frequent and intense wildfire activity. According to the wildfire statistics of National Interagency Coordination Center, the number of annual wildfires has decreased slightly over the last 5 years, but the number of acres impacted generally has increased, which indicates that the wildfire, on average, becomes larger. The buoyant wildfire smoke columns generate plumes that break through the atmospheric boundary layer (BL) and are transported hundreds to thousands of kilometers downwind (Damoah et al. 2004; Duck et al. 2007; Wandinger et al. 2002; Müller et al. 2005; Baars et al. 2021). In contrast, smoke plumes remaining within the BL often become well mixed in regions near the fire (Trentmann et al. 2002). The wildfire smoke is a complex mixture of pollutants that can undergo physical and chemical transformation processes during transport and can have major impacts on air quality and public health over vast geophysical areas (Teakles et al. 2017; Garofalo et al. 2019). Smoke particles can also affect climate by strong solar absorption (as the direct radiative effect; Ditas et al. 2018; Hirsch and Koren 2021) and by acting as cloud condensation nuclei (CCN) and ice-nucleating particles (INPs) in cloud evolution processes (as the indirect radiative effect; Knopf et al. 2018; Ansmann et al. 2021).

Numerical models are essential for predicting fire behavior, and better simulations will improve fire management and public safety. However, the fire smoke prediction depends on the accurate observational characterization of smoke plumes and their vertical structure. First, all chemical transport models require an estimate of the vertical distribution of smoke particles near the emission source (Trentmann et al. 2002; Reid et al. 2009; Sessions et al. 2011; Paugam et al. 2016; Moisseeva and Stull 2021). The buoyant rise and the resultant vertical distribution of wildfire smoke in the atmosphere have a strong influence on downwind pollutant concentrations at the surface. Second, the amount of smoke injected at different

Corresponding author: Min Deng, mdeng2@uwyo.edu

DOI: 10.1175/JTECH-D-21-0092.1

heights is a key input into chemical transport models and smoke modeling frameworks. The injection height influences plume transport characteristics such as smoke transport range/height and dilution potential and is therefore important for modeling wildfire smoke plume transport, footprints, and surface concentrations (Reid et al. 2009; Das et al. 2017). Additionally, injection height depends on the wind, turbulence, and other atmospheric conditions that the plume experiences. Peterson et al. (2014) found that an optimal method for predicting high-altitude injections requires the combination of injection climatology, fire radiative flux, and meteorology, but that each variable's importance depends on fire event characteristics.

Smoke injection heights have been studied from several satellite observations, namely, the Multiangle Imaging SpectroRadiometer (MISR; Diner et al. 1998), the Cloud–Aerosol Lidar with Orthogonal Polarization (CALIOP; Winker et al. 2010, 2013; Amiridis et al. 2010; Gonzalez-Alonso et al. 2019), and the recently launched Tropospheric Monitoring Instrument (TROPOMI; Griffin et al. 2020). From the MISR instrument on board the NASA Earth Observing System *Terra* satellite during the fire seasons of 2002 and 2004–07, Val Martin et al. (2010) found out that a significant fraction (4%–12%) of plumes from fires are injected above the BL. Most of the plumes located above the BL (>83%) are trapped within stable atmospheric layers. Griffin et al. (2020) evaluated the TROPOMI with MISR and CALIOP observations. The comparison between TROPOMI and MISR plume heights shows that, on average, the TROPOMI aerosol layer heights are lower, by approximately 600 m, compared to MISR, which is likely due to the different measurement techniques. The comparison to CALIOP shows that the TROPOMI aerosol layer height is more accurate over dark surfaces, for thicker plumes, and plumes between approximately 1 and 4.5 km. Despite of the discrepancy among those observations, they provide a climatological report of global wildfire plume injection heights.

However, the fire injection height may change as the fire intensity and its environment change, which is a complex interactive process. To provide a process-level observation of fire injection height, a field campaign with extensive in situ and remote sensing measurements would be more suitable for this subject. The focus of this study is on the wildfire smoke observations by the airborne Wyoming Cloud Lidar (WCL) during the Biomass Burning Flux Measurements of Trace Gases and Aerosols (BB-FLUX) project (R. Volkamer et al. 2022, unpublished manuscript). Section 2 describes the WCL measurement and auxiliary data. Section 3 introduces the WCL standard and scientific data processing. Section 4 presents the aerosol extinction coefficients retrieval from WCL measurements and its evaluation with coincident in situ aerosol and carbon monoxide (CO) concentration, and with column CO measurement on board the University of Wyoming King Air (UWKA). Section 5 contains a brief overview of the WCL observed smoke aerosol and a summary of the preceding sections, and the outlook for Deng et al. (2022, hereafter Part II).

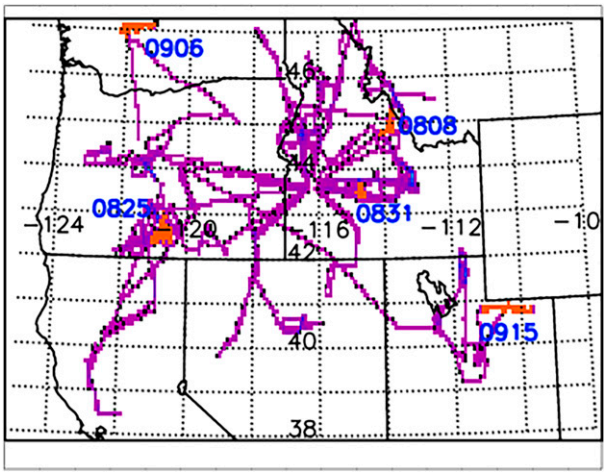

FIG. 1. The UWKA flight track distribution during the BB-FLUX project. The five fire plumes highlighted in red are the cases whose vertical structures are reconstructed with WCL transects to study the plume inject height in Part II.

2. Description of measurements during BB-FLUX

The 2018 BB-FLUX airborne field campaign explored synergistic benefits of remote sensing and in situ observations from the UWKA aircraft to quantify total emission and evolution of wildfire smoke plumes over the western United States. A detailed description of the scientific objectives, experiment design, instrument and modeling resources, and initial results are presented in R. Volkamer et al. (2022, unpublished manuscript). Briefly, over the course of 35 research flights, the BB-FLUX campaign sampled smoke from 20 wildfires in addition to aged regional smoke. Figure 1 shows a map of the UWKA flight tracks. The five regions with red colors indicate the frequently sampled plumes by the UWKA aircraft, which will be investigated in Part II. The UWKA flight tracks include parts of Washington, Oregon, Northern California, Nevada, Utah, Idaho, and western Montana; the sampled fire plumes are therefore representative of wildfires in the western United States. The UWKA flight pattern included a general surveillance of plume structure above the fires, followed by a series of flight legs oriented perpendicular to the mean low- to mid-level wind direction to best determine fluxes of trace gases and aerosols. Compared to the ground-based and satellite measurements, the UWKA aircraft is a flexible platform that enables smoke plume sampling at multiple altitudes to observe internal vertical structure with remote sensing and in situ measurements. As seen in Fig. 2, 70% of flight altitude is spent below 3 km AGL with flights up to 6 km to sample the top of some deep smoke plumes. The height from now on is above mean sea level.

a. Remote sensing measurements

1) AIRBORNE WCL MEASUREMENTS

The upward WCL is a compact two-channel elastic lidar with depolarization measurement. With the size, pulse energy,

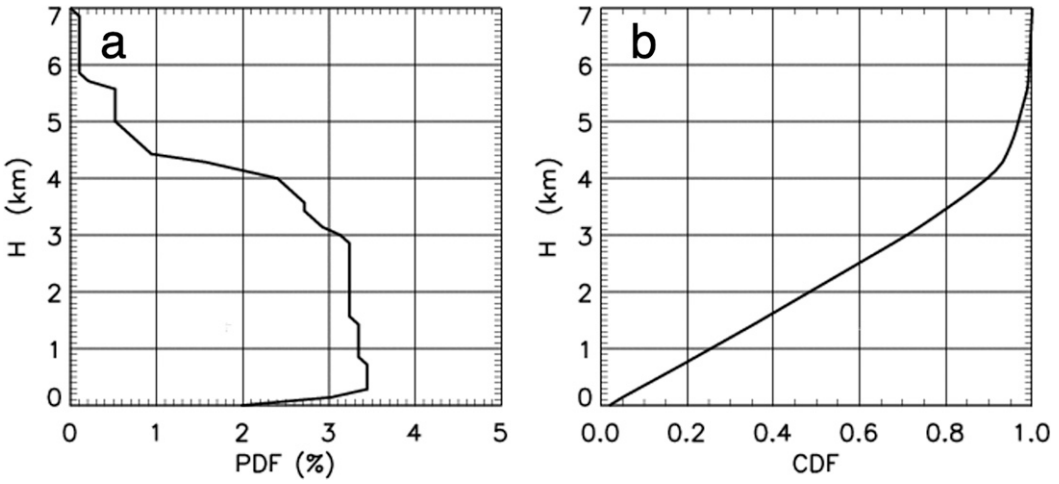

FIG. 2. The (a) PDF and (c) CDF of UWKA flight heights above the ground level (AGL) during the BB-FLUX project.

and eye safety of the laser for aircraft installation in mind, a small telescope of 10-cm diameter combined with a relatively high pulse-energy laser is used: Ultra Pulsed Nd:YAG Laser from the Big Sky Laser Technologies, Inc. It provides 20-Hz and 16-mJ output at 355 nm. This wavelength not only makes it easy to achieve eye-safe operation, but also provides a stronger molecular backscatter signal than a lidar operating at 532 or 1064 nm with the same laser energy. This is important for calibrating backscatter coefficients. The laser beam is expanded 5 times to a diameter of 15 mm before entering into the atmosphere, making the system eye safe beyond a distance ~65 m. For more details about WCL system specifications and its applications, please refer to Wang et al. (2009). WCL linear depolarization ratio measurements provide important information on aerosol particle shapes, especially when combined with backscatter intensity. Aerosol extinction coefficient can also be retrieved from WCL measurements by applying an effective backscatter to extinction ratio (lidar ratio, S) during the postproject processing of the lidar measurements. The WCL is sensitive enough to provide high spatial resolution measurements of boundary layer aerosols, which, in turn, provides new opportunities for boundary layer aerosol studies.

2) CU AIRSOF MEASUREMENTS

The University of Colorado Airborne Solar Occultation Flux (CU AirSOF) instrument measures column concentration of trace gases and quantifies trace gas fluxes with the UWKA wind data during the underpass plume aircraft transects (R. Volkamer et al. 2022, unpublished manuscript; Bela et al. 2022). It consists of a custom-built, motion-stabilized digital solar tracker coupled to a Fourier transform infrared spectrometer (FTS). An early version of the instrument is described in Kille et al. (2017) and the first measurements of CO from wildfires are shown in Bela et al. (2022). CU AirSOF measurements use direct sunlight to measure trace gas columns at midinfrared wavelengths. The UWKA flight tracks were designed to position the aircraft below the fire plume. The solar tracker uses an internal GPS unit to calculate the sun's position in the sky at the current time and position (Baidar et al. 2016). Using an image of the solar disk, custom LabView motion compensation software maintains sun tracking while the airplane is in flight. Infrared and visible wavelength cameras simultaneously image the sun, enabling solar tracking through optically thick overhead smoke plumes and cirrus cloud cover.

The FTS has spectral resolution of 0.5 cm^{-1}, and two detectors observe the spectral range from 700 to 5000 cm^{-1} (Kille et al. 2017). Four scans are coadded internally and stored to disk every 2 s. Species measured in the infrared include CO, NH_3, C_2H_6, and C_2H_4 using the SFIT4 software package. More details are provided in Kille et al. (2020).

b. In situ measurements

The atmospheric state measurements on board the UWKA aircraft during BB-FLUX include temperature, pressure, humidity, wind speed, wind direction, and turbulence.

1) THE PCASP

The Passive Cavity Aerosol Spectrometer Probe (PCASP) employs a He–Ne laser (λ = 0.633 μm) to size and count particles with diameters between 0.1 and 3 μm (Cai et al. 2013). Mie scattering theory (Twomey 1977, 199–217) was used with an assumed particle refractive index (1.59 + 0.00i) to convert scattered light intensity into particle diameter (D, assuming spherical particle shape). The PCASP calibration procedure is described in Cai et al. (2013). The relationship between intensity and D and recordings of the particle count histogram and sample flow rate were used to calculate an aerosol size distribution. The latter were used to calculate aerosol number concentration, aerosol surface area concentration, aerosol volume concentration, and mean particle diameter. During BB-FLUX, two PCASPs (PCASP-2, SN = 39798-0200-26; PCASP-1, SN = 1013-0502-29) were deployed consecutively

on the UWKA. Although the two PCASP instruments were both calibrated in the laboratory prior to deployment, postcampaign data analysis showed a significant disagreement between the two instruments. Following analysis described in a supplement (http://www-das.uwyo.edu/~jsnider/pcasp_measurement_processing_v4.pdf), measurements from PCASP-1 acquired after 12 August were used to construct correlations among the WCL-derived aerosol extinction coefficient and the three PCASP-derived concentrations (i.e., aerosol number, aerosol surface area, and aerosol volume).

The presence of multiple particles within the PCASP sample volume (coincidence) is known to result in biased values of aerosol number concentration and aerosol volume concentration. This was investigated using PCASP measurements (PCASP-1 and PCASP-2) acquired during King Air transits of a wildfire smoke plume and using laboratory-based characterizations of the PCASPs. Within the plume, the PCASP-derived number concentration maximized at ~8000 cm^{-3}. The effect of coincidence bias [Willeke and Liu 1976, their Eq. (2)] was estimated to be 5% and 2% for aerosol number concentration and aerosol volume concentration, respectively.

2) AERO-LASER 5002 CO MEASUREMENT

The NCAR/NSF Aero-Laser 5002 CO fluorescence instrument is a commercial version of the instrument published by Gerbig et al. (1999). The source is a flowing resonance fluorescence discharge gas lamp emitting in the resonance fluorescence in the fourth positive band of CO. An optical filter provides a narrow band of source radiation centered at 151 nm with a 10-nm bandpass. CO fluorescence is detected using photon counting. The internal data system can accommodate sampling rates from 1 to 18 samples per second. In-flight calibrations are conducted using a working standard and a catalytically scrubbed zero trap for background subtraction. A series of primary standard compressed gases are used in laboratory measurements to quantify the concentration of the working standard cylinder. Two to three replicates of these standardizations are conducted prior to and after the intensive field phase of the experiment. Additional characterizations are performed as needed upon replacement or refilling of the working standard cylinder. The CO mixing ratio in ppbv is recorded. Its precision is 2 ppbv for a 10-s averaging time.

To convert the CO unit from ppbv to molecules per cubic centimeter (molecules cm^{-3}) in this study, the number of moles per liter in air at 1-atmosphere pressure and 298 K is given by

$$n/V = P/RT,$$

where n is molar number, V is volume, P is pressure, R is 0.08 206 L atm K^{-1} mol^{-1}, and T is temperature. Not that 1 ppbv at 1-atmosphere pressure and 298 K is 2.46×10^{10} molecules cm^{-3}. To account for the density variation with pressure and temperature, the conversion is multiplied by $P/(1\ \text{atm}) \times (298\ \text{K})/T$.

3. WCL data processing

As the laser pulse travels along, part of it is scattered by molecules, water droplets, or other objects in the atmosphere. A small portion of the scattered light is scattered back, collected by the telescope, and detected by the photomultiplier tubes (PMT). The detected signal is stored in bins according to how long it has been since the pulse was transmitted, which is directly related to how far away the backscatter occurred. The collection of bins for each pulse is called a profile. The following instrument-level corrections are required to produce the standard level 0 and level 1 data.

a. Background noise correction

Background noises due to the sunlight at 355 nm and the PMT noise are collected in addition to atmospheric backscatter signal, and they need to be subtracted. As the WCL is designed, pretrigger values (data before the laser pulse is transmitted) are recorded for the background noise correction. We can also use the far range data for subtraction assuming no atmospheric signal. In the BB-FLUX data processing, we use the far range (9–10 km) data. First, there are no clouds observed 10 km above mean sea level during BB-FLUX. Second, the measured clear-sky backscatter signal after noise correction is parallel to the simulated atmospheric Rayleigh scattering, therefore the ratio between the measured clear-sky backscatter to the simulated atmospheric Rayleigh scattering in Fig. 3a is constant with range above 0.5 km, which indicates that no additional atmospheric backscatter signal is subtracted using the far range data.

b. Overlap factor correction

Overlap factor correction is applied as a function of range to account for loss in the near-field receiver efficiency, which is deliberately minimized to avoid the detector saturation from strong lidar signal. Prior to the BB-FLUX project deployment, the WCL was aligned and tested in the test flights. After the alignment, the UWKA flew above the BL to observe the clear sky for 10 min. Figure 3 shows the WCL overlap factor generated for BB-FLUX with the 10-min clear-sky WCL measurement on board of UWKA flying at 5 km. The clear-sky signal after noise correction is normalized with the simulated atmospheric Rayleigh scattering in Fig. 3a, the inversion of which is the overlap factor, shown in Fig. 3b. We can see that the overlap factor is close to 1 at about 0.5 km. Below that height, the overlap factor increases with decreasing height. Figures 3c and 3d show the averaged WCL backscatter coefficient and depolarization ratio over the 10-min in solid black lines, respectively. The dotted blue lines are two random profiles in the 10-min measurement to show the signal standard deviation. The minimum height level or blind zone of WCL measurement is 75 m. In the unlikely event that lidar alignment is lost during the field deployment, a new set of overlap factors is generated using a new 10-min of WCL measurement collected above the boundary layer in the molecular scattering condition after realignment.

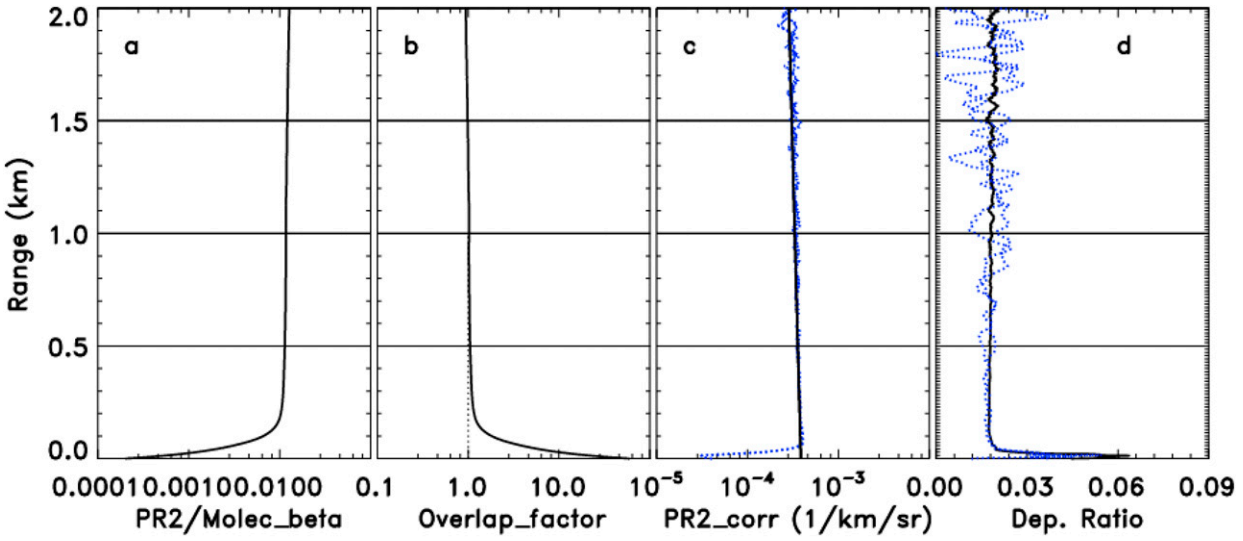

FIG. 3. WCL overlap factor correction with simulated molecular backscatter signal and 10-min clear sky WCL measurement on board of UWKA flying at 5km. (a) Averaged profile of the ratio of the measured backscatter over the simulated molecular backscatter, (b) overlap factor from this 10-min sample, (c) measured clear-sky backscatter coefficient after overlap factor correction, and (d) depolarization ratio. Black solid line in (c) and (d) are 10-min average, and blue dotted lines are two random profiles in the 10-min measurement.

c. Range-square correction

The PMT signal needs to be range corrected to derive backscatter coefficients of the atmospheric scatters. As the range increases, the noise residue in the signal also increases in the range-square correction, resulting in a decreased signal-to-noise ratio (SNR), which are shown in the dotted blue lines in the Figs. 3c and 3d.

d. LDR calibration

To improve lidar linear depolarization measurements, a half-λ wave plate is placed after the beam expander and coupled with a cubic polarization beam splitter in the receiver path to split the received backscatter light into parallel and perpendicular channels. During the lidar depolarization ratio (LDR) test in the lidar laboratory, the offset angle between the half-wave plate and the cubic polarization beam splitter is adjustable with 1° steps. The WCL calculated LDR of variant offset angles (diamonds in Fig. 4) are fitted with the simulated LDR (solid black line in Fig. 4) of clear sky to find the exact offset angle and the WCL LDR calibration constant. In this case, the offset angle is at 13°, and the calibration constant is 11.5. This simulation and fitting method can calibrate the polarization lidar well in the laboratory as shown in Fig. 4. For WCL installation on board the UWKA aircraft, another double-paned window is installed between the WCL and the aircraft ceiling for safety and to prevent possible frosting. The properties of the window depolarization under different atmospheric conditions are unknown. Therefore, this extra window may cause some bias in the WCL depolarization. However, we assume this bias is minimal. The averaged clear sky LDR of the 10-min WCL measurement in Fig. 3d is around 0.018. The standard deviation of LDR increases with height due to decreased SNR and even weaker SNR in the perpendicular channel. In thin smoke, the uncertainty of LDR at 2 km could be 100%, while in thick smoke, the error decreases significantly as the SNR increases by orders, which will be illustrated by the following case study in section 4. Up to now, the instrument-level correction procedures to generate the standard level 0 data have been introduced.

e. Attenuated backscatter coefficient calibration

To generate the standard level 1 data of calibrated attenuated backscatter coefficient, we simulated molecular range-

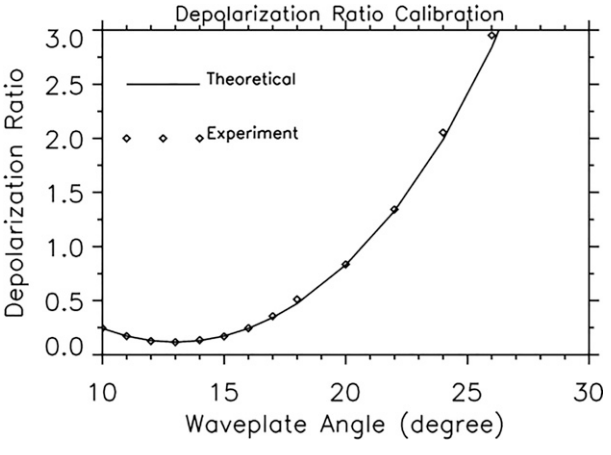

FIG. 4. WCL LDR calibration. The solid line is the theoretical calculation of LDR as a function of wave-plate angle and LDR calibration constant. The diamonds are the WCL measured LDR during the WCL laboratory experiment with different wave-plate angles.

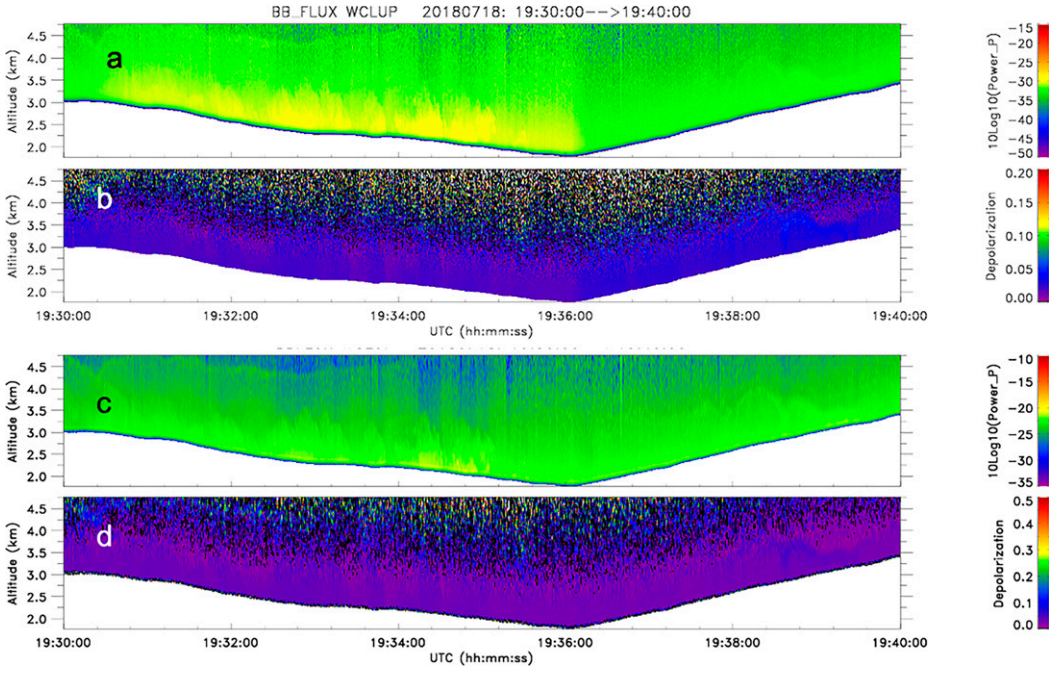

FIG. 5. An example of attenuated backscatter coefficient calibrations. WCL-measured attenuated backscatter coefficient and depolarization ratio (a),(b) before the calibration and (c),(d) after the calibration. Please note that the color bar ranges of data before and after the calibration are different.

corrected backscatter profiles using in situ measurements of temperature and pressure at the flight level, assuming standard atmospheric profiles. The calibration factor is the ratio of the simulated molecular backscatter and the WCL clear sky measurement. Due to the decreased SNR with range, the calibration factor is averaged between 1- and 3-km range and above boundary layer to avoid significant noise effect and low-level aerosol contamination.

Variation in the calibration factor can be significant due to laser variations and flight situation. Figures 5a and 5b show the WCL uncalibrated backscatter coefficients and depolarization ratio (level 0 data). The WCL received backscatter coefficients decrease by about 3 dB when the UWKA aircraft starts to ascend. Similar fluctuations in backscatter coefficients with UWKA ascents and descents were observed throughout the BB-FLUX campaign. To correct these fluctuations, a method was developed, which correlates the WCL backscatter coefficients at three different altitudes (0.5, 1.0, and 1.5 km). This method assumes that fluctuation in the whole profile is significant enough that the calibration factors at different altitudes are highly correlated. This method is not applicable in cases where the WCL backscatter signal is quickly attenuated, as in thick smoke. Fortunately, the UWKA aircraft only made sharp ascending or descending changes while outside of smoke plumes. The final calibrated attenuated backscatter coefficient and LDR (level 1 data in different color scale) are shown in Figs. 5c and 5d. The overall system uncertainty is estimated to be less than about 2 dB.

4. Extinction coefficient retrieval and evaluation

An example of attenuated backscatter coefficients and LDR observed by the WCL inside a smoke plume from the Rabbit Foot fire in eastern Idaho during RF09 on 8 August 2018 is shown in Figs. 6a and 6b. First, the outlines of the attenuated backscatter and LDR at 4.5–5.5 km are correlated with each other. The LDR reveals the physics between the depolarization of linearly polarized light and smoke aerosol shape and size. The smoke LDR is larger than marine aerosol but smaller than dust aerosol. With CALIOP observation, Kim et al. (2018) also showed that the smoke aerosol particulate depolarization ratio is generally less than 0.15, but can be as larger at 0.4 in depolarizing smoke layer. Second, the attenuated backscattering in Fig. 6a shows that there is a layer of prevailing background smoke below 4.5 km at −35 dB in green color. Around 2153 UTC, the UWKA flew through the center of the fire plume, where the lidar signal is attenuated in less than 500 m by the thick plume. This limited penetration is the limitation of lidar observation. Fortunately, the flight plan during BB-FLUX allows the WCL to sample the same smoke plume at several height levels, which allows us to reconstruct and examine the smoke plume vertical structure. Prior to 2153 UTC, the base of the smoke plume was clearly detected as extending from flight level to 5 km altitude for a period of less than 30 s, which corresponds to about 3-km horizontal distance. After 2153 UTC, the backscatter signal is quickly attenuated from −30 dB at the near-flight level to the −35 dB, which renders it difficult to differentiate between the

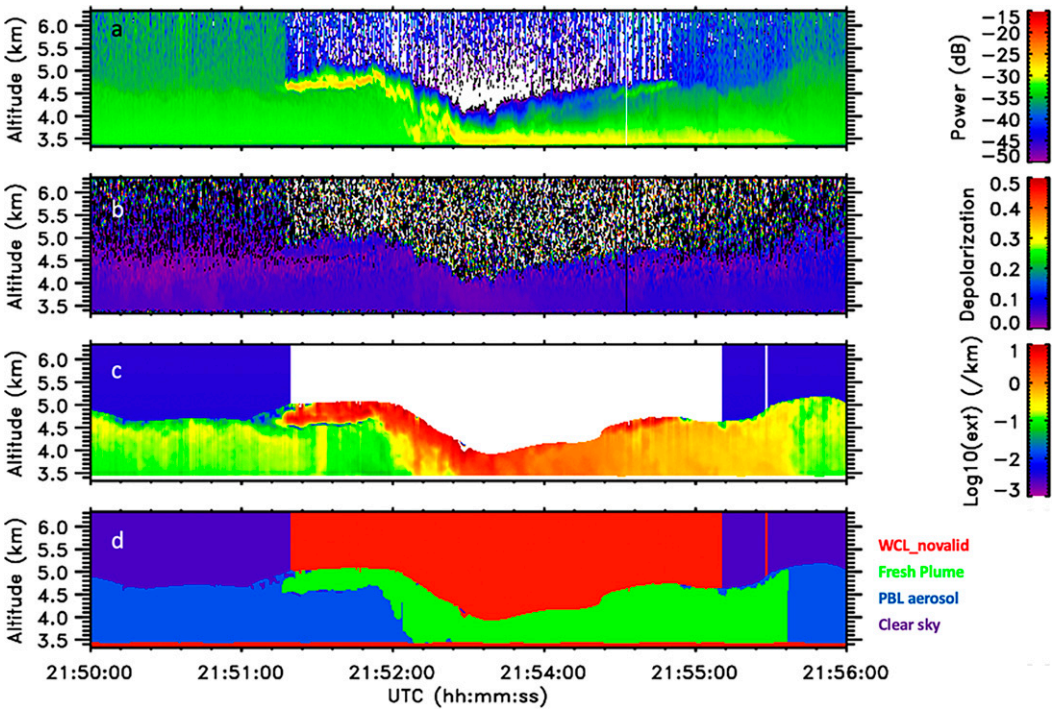

FIG. 6. (a) The WCL-measured attenuated backscatter coefficient, (b) linear depolarization ratio, (c) retrieved extinction coefficients, and (d) the mask on 8 Aug 2018. In (d), green is the fresh fire plume, blue is old boundary layer aerosol, purple is clear sky, and red is the region that WCL is either fully attenuated or the near range. This event is coded as RF09-02-10_PUN_C_04 (RF09, second section, tenth event in that section, plume underpass for column measurements, the fourth underpass) in the archived dataset, which will be introduced in more detail in the BB-FLUX overview paper in R. Volkamer et al. (2021, unpublished manuscript).

localized smoke plume and regional background smoke. Therefore, we utilize an extinction coefficient retrieval method in the following to get rid of the attenuation in WCL signal, which will help us to distinguish the thin background smoke and fresh thick smoke.

a. Fernald iteration retrieval method

The aerosol extinction coefficient profiles are retrieved using the Fernald's method (Fernald 1984) with backward iteration. This method has two critical assumptions. First is the aerosol extinction-to-backscatter ratio, or lidar ratio, S_a. A review on smoke lidar ratios and depolarization ratios in the troposphere and stratosphere can be found in Haarig et al. (2018) and Müller et al. (2007). The observed lidar ratio for aerosol varies from 10 to 100 sr depending on the aerosol type and the lidar wavelength (Anderson et al. 2000; Ackermann 1998; Wandinger et al. 2002). A good estimate for the 355-nm smoke lidar ratio is probably 50 sr. Haarig et al. (2018) published 355 nm lidar ratio values for Canadian smoke, for the smoke in the troposphere and in the stratosphere. The biomass burning cluster of AERONET measurements is used to model the CALIOP smoke aerosol. Cluster analysis of the AERONET data yields S_a values of 70 sr at 532 nm and 40 sr at 1064 nm. These values compare well with the 532-nm measurements of Ansmann et al. (2001) of 70 sr for biomass burning–influenced aerosol advected from the Indian subcontinent during the Indian Ocean Experiment (INDOEX) and with Voss et al. (2001) of 60 ± 6 sr off the west coast of Africa. Cattrall et al. (2005) report values of 71 sr at 532 nm from their AERONET study. Ohneiser et al. (2020) reports typical values and spectral dependencies of the lidar ratio and linear depolarization ratio for aged stratospheric smoke from Australian wildfires. At 355 nm, the lidar ratio ranged from 53 to 97 sr. At 532 nm, the lidar ratios were higher (76–104 sr), and the depolarization ratios were lower, with values around 0.15. The observed lidar ratio and depolarization ratio for Australian smoke agree well with those obtained from observations of stratospheric smoke layers over central Europe in summer 2017 (originating from record-breaking Canadian wildfires). The higher 532-nm lidar ratios, however, indicate stronger absorption by the Australian smoke particles. In this study, we used a lidar ratio of 60 sr.

It is well known that boundary conditions are important for deriving aerosol extinction coefficient profiles from lidar return signals using the popular Fernald's method. In this study we used a simple lidar scattering ratio, the ratio of WCL measured attenuated backscatter to the simulated molecular backscatter, to identify the aerosol. This mask method, compared with the slope method in Wang and Sassen (2001), may lose sensitivity when the WCL is attenuated down to the noise level.

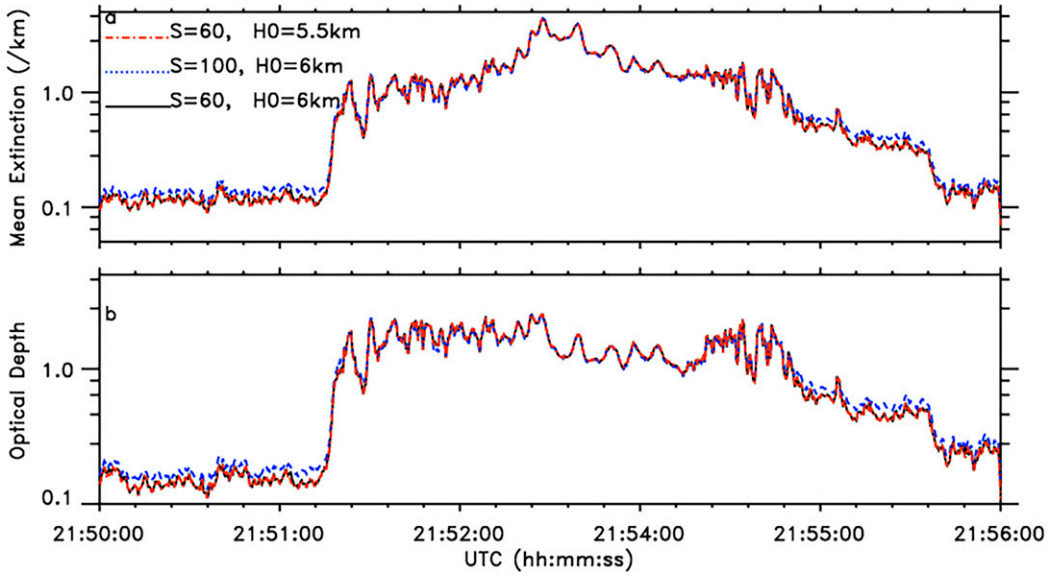

FIG. 7. The WCL-retrieved (a) layer-mean extinction coefficients and (b) aerosol optical depth for the case in Fig. 6. The retrieved sensitivity tests in different colors are based on different lidar ratio (S) and the reference height level (H0).

The retrieved aerosol extinction coefficients of smoke observed in Fig. 6a are shown in Fig. 6c. The sensitivities of retrieved layer mean extinction coefficients and aerosol optical depth to lidar ratio and boundary heights are shown in Fig. 7, which shows little sensitivity to the lidar ratio and boundary height, probably due to the convergence of Fernald backward iteration and the high SNR in the smoke. The mean extinction coefficients increase from about 0.1 km^{-1} at both sides to about 3 km^{-1} at the plume center where WCL signal is attenuated within 500 m. A threshold of 0.2 km^{-1} is used to distinguish the dense localized fresh smoke from the aged background smoke, the resulted mask of fresh plume is shown green in Fig. 6d. The average extinction profiles of biomass burning aerosol from the global CALIOP measurement (Yu et al. 2010) is less than 0.2 km^{-1}. One thick smoke case in Wandinger et al. (2002) has extinction coefficient larger than 0.2 km^{-1}.

The background smoke has extinction coefficients around 0.1 km^{-1}, shown in blue in Fig. 6d. Within the background smoke layer, a denser fresh smoke plume is observed in green in Fig. 6d. The smoke plume is asymmetrically detrained from the center to both sides. On the left-hand side, the smoke plume has a clearly defined top above the boundary layer, which extends from UWKA flight level at 2152 UTC to 5 km; this may be a good indicator of plume injection height. On the right-hand side, the smoke plume appears to be mixed into the boundary layer. The attenuated backscatter coefficients suffer from two-way attenuation, which decreases the backscatter coefficient in dense smoke, and smears the contrast between the dense fire plume and background aerosol layer. After subtracting the two-way attenuation, the retrieved aerosol extinction coefficient in Fig. 6c in fresh smoke is 2–10 times larger than the background smoke.

b. Evaluation with PCASP and CU AirSOF measurements

Although there are no collocated in situ aerosol extinction coefficient measurements to evaluate the WCL retrieval, the PCASP operated on the UWKA measured aerosol number, surface area, and volume concentrations. We evaluated the mean WCL extinction coefficients between 75 and 150 m of the UWKA flight level with in situ PCASP data. The joint probability density functions (PDFs) are plotted in Figs. 8a, 8b, and 8c. The WCL extinction coefficients increase as the PCASP values increase, indicating a positive correlation between lidar-derived aerosol extinction coefficients and PCASP values. However, the deviation between the WCL and PCASP increases as the WCL extinctions decrease, which may be a result of different instrument sensitivities in low aerosol regimes. Figure 5d shows the joint PDF distribution of NCAR CO concentration and WCL extinction coefficients. The NCAR in situ CO concentration ranges from 50 to 2000 ppbv and increases monotonically with the WCL extinction coefficient. The correlation coefficients in Fig. 8 are larger than 0.8. The majority of the observed smoke has extinction coefficients ranging from 0.1 to 1.0 km^{-1} and aerosol number concentrations from 500 to 5000 cm^{-3}. In these regions, the relations between the WCL extinction (σ) and the in situ variables (y) are almost log-linear or power-law relationship ($y = a\sigma^b$).

Based on the AERONET database, Ansmann et al. (2021) studies conversion factors used to convert the optical measurements into microphysical properties such as the aerosol particle mass, volume, surface area, and number concentration from backscatter lidar measurements on the ground and space. The application of the conversion method shows the potential of spaceborne and ground-based lidars to document large-scale and long-lasting wildfire smoke events in detail

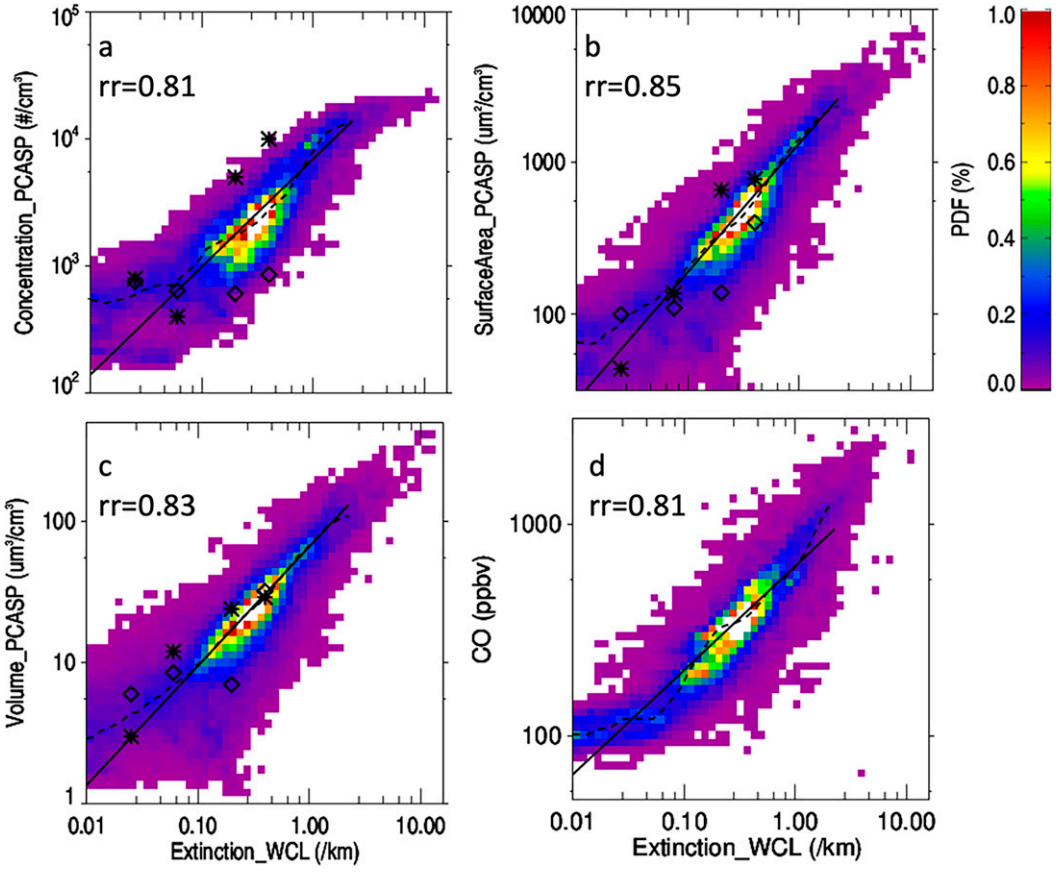

FIG. 8. The correlated PDFs of WCL retrieved extinction coefficient at the flight level vs PCASP-measured (a) aerosol number concentration, (b) surface area concentration, (c) volume concentration, and (d) NCAR CO concentration for the data collected during 14 Aug–17 Sep 2018. The corresponding correlation coefficient (rr) between the in situ measurement and the WCL retrieved extinction coefficient is captioned in each panel. The dashed line represents the PDF mode within the given WCL retrieval aerosol extinction coefficient bins. The PDF mode value and the extinction coefficient bins are listed in Table 1. The solid lines represent the fitted power-law relations, whose coefficients are listed in Table 2. The aerosol number, surface area, and volume concentration from lidar retrieval and in situ measurement in Wandinger et al. (2002) are shown in diamond and asterisk symbols, respectively, in Figs. 8a–c.

and thus to provide valuable information for climate, cloud, and air chemistry modeling efforts performed to investigate the role of wildfire smoke in the atmospheric system. In this study, we also develop the conversion based on the collocated WCL extinction coefficient and in situ measurements at flight level in Fig. 8. First, the PDF mode (black dash line) and standard deviation within the given WCL retrieval aerosol extinction coefficient bins are provided in Table 1. Second, the power-law relationship (solid black line) are fitted in Fig. 8. The fitted power-law coefficients are listed in Table 2. The conversion factor in Ansmann et al. (2021) is based on a linear relationship and the extinction coefficients are very smaller compared to the data in this study, so it is not compared with our results. But the aerosol number, surface area and volume concentration from lidar retrieval and in situ measurement for two-case study in Wandinger et al. (2002) are shown in diamond and asterisk symbols in Fig. 8. The comparison shows that there is a positive correlation between the results in Wandinger et al. (2002) and the data collected during BB-FLUX. The results of this study in Fig. 8 are within the deviation between the lidar retrieval and the in situ measurement in Wandinger et al. (2002).

One application of this conversion is to provide profiles of aerosol number, surface area, and volume concentration, CO concentration from the WCL retrieval, from which the column concentration can be derived by integrating the converted concentration profiles. The CU AirSOF measures the column-integrated CO concentration. The comparison of the WCL-derived CO columns and CU AirSOF measured CO columns for the flight on 8 August 2018 is shown in Fig. 9, along with the flight altitude, layer mean extinction coefficients, WCL penetration depth, and WCL-derived aerosol optical depth. The WCL-derived CO columns and the CU AirSOF measured CO columns show very similar temporal variations. There are eight WCL transects. The yellow boxes denote the five underpasses at about 2 km, the two red boxes

TABLE 1. List of the PDF mode value/standard deviation of the PCASP aerosol number, surface area, and volume concentrations, NCAR CO concentration, and its corresponding extinction coefficient bins in Fig. 8 for converting the WCL-retrieved extinction (σ) to aerosol number, surface area, and volume concentrations, and CO concentration.

Extinction (km^{-1})	Aerosol number concentration (cm^{-3})	Aerosol surface concentration (μm^2 cm^{-3})	PCASP aerosol volume concentration (μm^3 cm^{-3})	NCAR COconcentration (ppbv)
0.012	543/67	71/11	3/1	196/16
0.027	625/111	91/18	4/1	225/21
0.056	828/145	101/25	6/2	230/16
0.065	719/176	115/29	6/2	228/22
0.102	1264/174	184/29	8/2	320/18
0.139	1456/189	262/31	12/2	349/19
0.188	1676/193	331/34	16/2	579/22
0.218	1930/194	331/30	18/2	581/19
0.254	1677/205	372/32	19/2	585/20
0.294	1930/208	373/33	23/2	588/19
0.343	2223/201	471/33	24/2	631/18
0.398	2559/234	371/47	27/2	633/21
0.463	2947/299	596/47	30/3	687/25
0.538	3393/353	754/63	34/3	811/28
0.625	3907/412	754/68	39/4	813/32
0.726	3907/483	1073/93	51/5	1047/42
0.844	9102/887	1206/105	58/6	1141/49
0.981	9103/745	1357/105	65/6	1143/59
1.141	10 481/842	1526/113	74/6	1143/63
1.326	10 486/823	1526/124	85/7	1224/69
1.541	11 001/840	1716/142	96/8	1742/78
2.081	13 895/1075	2442/182	109/9	2244/103
2.811	13 895/921	2571/210	109/11	2442/96
5.131	18 420/779	3473/256	159/16	3148/102

are the plume intercepts at about 5 km, and the blue box is the transect at 3.5 km shown in Fig. 6. For the five underpasses, the Air SOF CO column concentrations maximize at about 5–8 $\times$ 10^{18} molecules cm^{-2}, while the WCL-derived CO columns maximizes at 3–4 $\times$ 10^{18} molecules cm^{-2}, because the WCL penetration depth is less than 1 km. For the two intercepts at about 5 km, the WCL penetration is at about 0.2–0.5 km with a mean extinction coefficient close to 5 km^{-1}, which is larger than that of the underpass transects, indicating the vertical variation of the plume property. The WCL derived and AirSOF CO column concentration are at about 3 $\times$ 10^{18} molecules cm^{-2}, indicating that the smoke plume top is around 5.5 km. When the UWKA aircraft is in relatively clean regions at the beginning and end of the flight legs, both the CU AirSOF measured and WCL-derived CO column are 1–2 $\times$ 10^{18} molecules cm^{-2}. Between 2140 and 2220 UTC, the UWKA flew three different flight levels along the similar flight track. Assuming that the WCL sampled three vertical segments of the same smoke plume during those 40 min, the summed WCL-derived CO column (7 $\times$ 10^{18} molecules cm^{-2}) agrees with CU AirSOF measurement (8.0 $\times$ 10^{18} molecules cm^{-2}) within 30% error at around 2140 UTC.

TABLE 2. The fitting coefficients of power-law relations ($y = a\sigma^b$) for converting the WCL retrieved extinction (σ in units of km^{-1}) to aerosol number, surface area, and volume concentrations, and CO concentration derived from data in Fig. 8.

	a	b
Aerosol number concentration (cm^{-3})	6549.01	0.847 991
Aerosol surface area concentration (μm^2 cm^{-3})	1238.48	0.842 627
Aerosol volume concentration (μm^3 cm^{-3})	62.2407	0.844 129
CO concentration (ppbv)	1103.98	0.491 779

5. Overview and summary of WCL observed smoke during the BB-FLUX campaign

The WCL-derived smoke vertical distributions for thick (blue), thin (red), and all (black) smoke are shown as solid lines in Fig. 10a. Between 2 and 5 km, where the majority of observed smoke resided, thin smoke is observed more often than thick smoke. Below 2 km and above 5 km, thin and thick smoke are observed equally often, even though in reality thin smoke should be more common due to regional transport. However, UWKA flights tended to target relatively fresh thick smoke over aged thin smoke. In Fig. 10d, the total aerosol concentrations of thin and thick smoke are shown in solid blue and red lines. The fraction of aerosol concentration from thin and thick smoke are plotted in dashed blue and red lines. Aerosol concentration contribution from thick smoke is about twice as that from the thin smoke.

The mean vertical profiles of depolarization and extinction coefficient of all, thin, and thick smoke, filtered using an extinction coefficient threshold of 0.2 km^{-1}, are shown in Fig. 10b. Thick smoke has a mean extinction coefficient

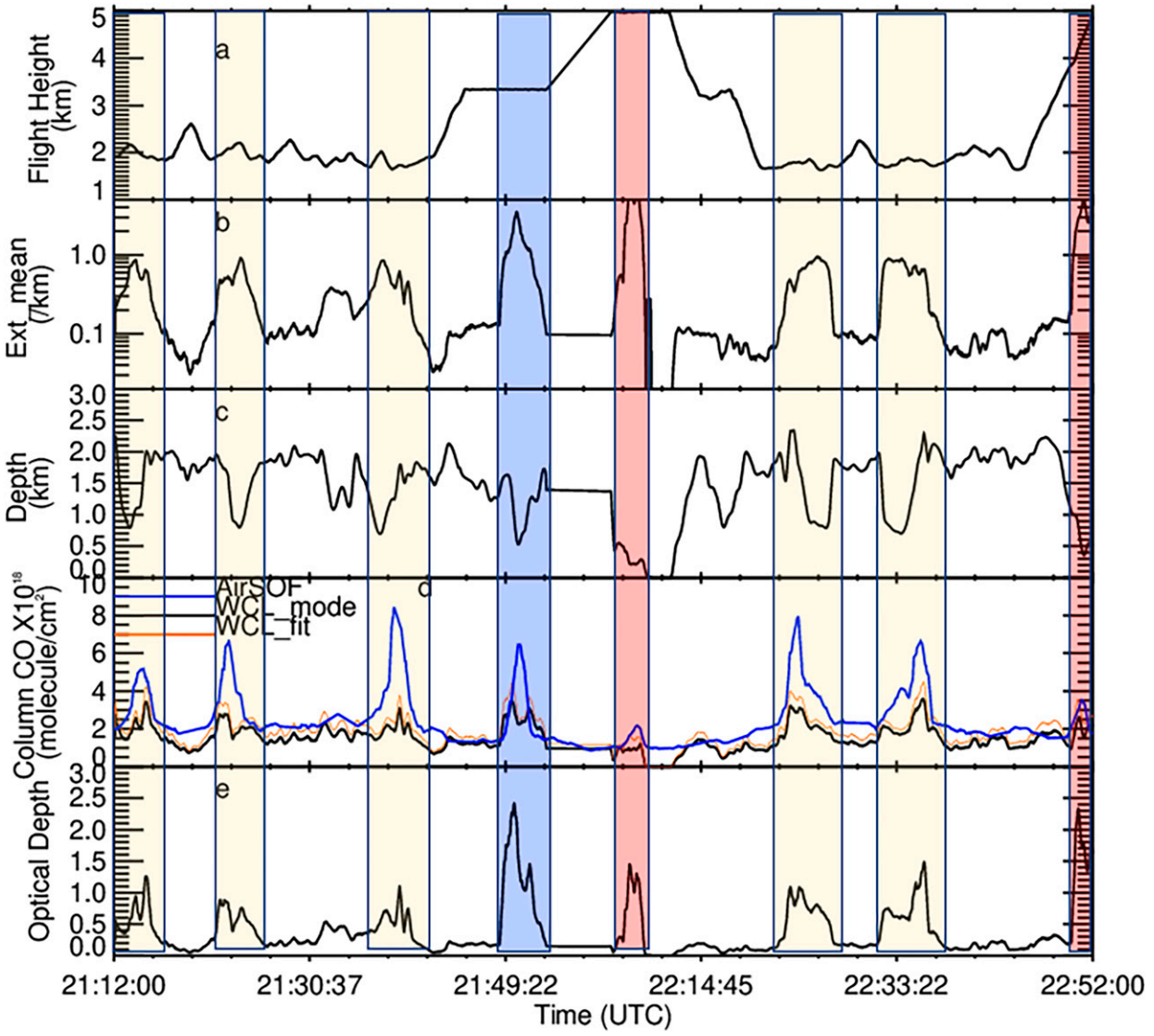

FIG. 9. The time series of (a) flight height, (b) layer mean extinction coefficients, (c) WCL penetration depth, (d) column CO concentration, and (e) WCL measured optical depth of the Rabbit Foot fire plume on 8 Aug 2018. In (d), the WCL-derived column CO concentrations from the PDF mode method (black line) and the power-law-fitting method (red line) are compared with the AirSOF measurements (blue line). The yellow boxes are the underpasses transects, and red boxes are the plume intercepts rather than underpass because most of the column was below the flight level. The blue box is the transect shown in Fig. 6.

ranging from 0.5 to above 1 km^{-1}, while thin smoke has a mean extinction coefficient of about 0.1 km^{-1}. Thick smoke also has a larger depolarization ratio, suggesting that the thick smoke may contain more irregular aerosol particles such as flying ash or dust, compared to thin smoke. Such irregular particles (Nisantzi et al. 2014) likely increase the depolarization in the fresh thick smoke, and then sediments during the transport. Wagner et al. (2018) and Adam et al. (2020) show the depolarization ratio is smaller for long-range-transported smoke, which is consistent with the results in this study.

This study described the generation of standard WCL L0 and L1 products such as calibrated attenuated backscatter coefficient during BB-FLUX. Scientific data products such as aerosol extinction coefficients are also retrieved using the Fernald method, assuming a constant lidar ratio. The retrieved aerosol extinction coefficients are compared with PCASP aerosol number, surface area and volume concentration and NCAR CO concentration at the UWKA flight level. The joint PDFs show strong correlations between WCL and in situ data and provide a first-order estimate for converting WCL extinction coefficients into vertical profiles of CO and aerosol concentration. The WCL-derived CO columns show a good agreement with the CU AirSOF measured CO columns in nonextinguished profiles, supporting the validity of the WCL-derived columns.

During the BB-FLUX airborne field campaign, the UWKA aircraft flew over U.S. western regions to sample fresh wildfire

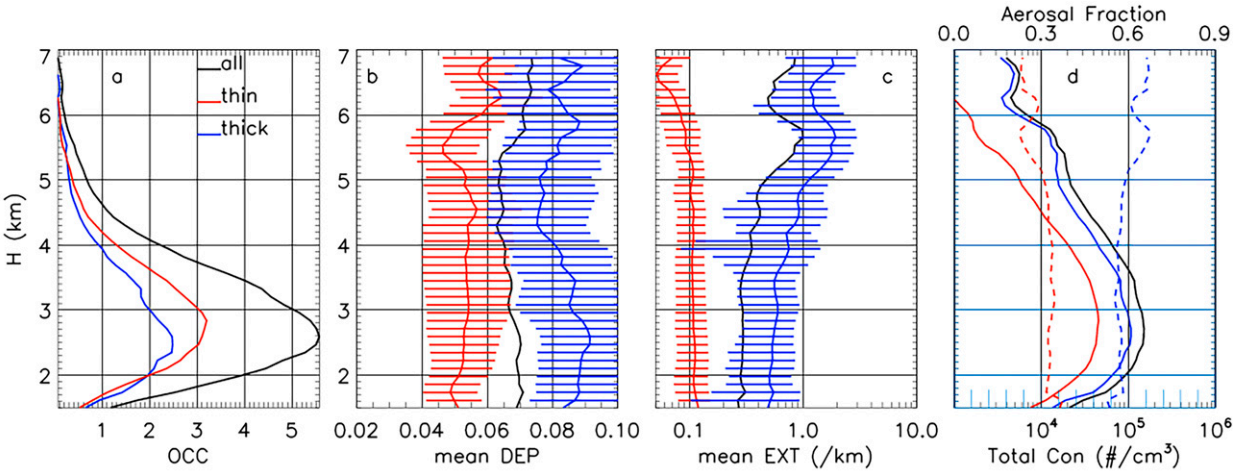

FIG. 10. (a) The WCL-measured fire smoke vertical occurrence, (b) mean depolarization ratio, (c) mean extinction coefficient, and (d) total aerosol concentration for all aerosol (black solid), and thick (blue solid) and thin (red solid) smoke. The dashed blue and red lines in (d) are the aerosol fraction of thin and thick smoke, respectively.

smoke plumes and regional background thin smoke for about 100 h. The retrieved extinction coefficients, after accounting for two-way attenuation in the smoke plume, provide a strong contrast between optically thick localized smoke and optically thin regional background smoke. Thin smoke should be spatially dominant due to transport and dilution, but due to targeted sampling, an almost equal amount of thin and thick smoke was observed above 5 km and below 2 km. Between 2 and 5 km, where the majority of the observed smoke resided, the WCL observed slightly more thin smoke than thick smoke. Extinction coefficients are 2–10 times larger in thick smoke than in thin smoke, and thick smoke tended to have larger depolarization ratios, presumably due to the presence of irregularly shaped aerosol particles such as flying ashes or dust. In Part II, the vertical structures of the fire plumes highlighted in Fig. 1 are reconstructed with consecutive WCL transects to investigate the plume internal variation and the plume injection height.

Acknowledgments. The 2018 BB-FLUX campaign is supported under U.S. National Science Foundation (NSF) Award AGS-1754019 (PI: Rainer Volkamer). The WCL data analysis is supported by University of Wyoming King Air corporative agreement funded by NSF. We also like to thank the University of Wyoming King Air team for the successful deployment of the project. The BB-FLUX remote sensing and in situ measurement and WCL data can be obtained from the UWKA project website (http://www.atmos.uwyo.edu/uwka/projects/index.shtml).

REFERENCES

Ackermann, J., 1998: The extinction-to-backscatter ratio of tropospheric aerosol: A numerical study. *J. Atmos. Oceanic Technol.*, **15**, 1043–1050, https://doi.org/10.1175/1520-0426(1998)015<1043:TETBRO>2.0.CO;2.

Adam, M., D. Nicolae, I. S. Stachlewska, A. Papayannis, and D. Balis, 2020: Biomass burning events measured by lidars in EARLINET—Part 1: Data analysis methodology. *Atmos. Chem. Phys.*, **20**, 13 905–13 927, https://doi.org/10.5194/acp-20-13905-2020.

Amiridis, V., and Coauthors, 2010: Smoke injection heights from agricultural burning in eastern Europe as seen by CALIPSO. *Atmos. Chem. Phys.*, **10**, 11 567–11 576, https://doi.org/10.5194/acp-10-11567-2010.

Anderson, T. L., S. J. Masonis, D. S. Covert, and R. J. Charlson, 2000: In situ measurements of the aerosol extinction-to-backscatter ratio at a polluted continental site. *J. Geophys. Res.*, **105**, 26 907–26 915, https://doi.org/10.1029/2000JD900400.

Ansmann, A., F. Wagner, D. Althausen, D. Muller, A. Herber, and U. Wandinger, 2001: European pollution outbreaks during ACE 2: Lofted aerosol plumes observed with Raman lidar at the Portuguese coast. *J. Geophys. Res.*, **106**, 20 725–20 733, https://doi.org/10.1029/2000JD000091.

——, and Coauthors, 2021: Tropospheric and stratospheric wildfire smoke profiling with lidar: Mass, surface area, CCN, and INP retrieval. *Atmos. Chem. Phys.*, **21**, 9779–9807, https://doi.org/10.5194/acp-21-9779-2021.

Baars, H., P. Seifert, R. Engelmann, and U. Wandinger, 2017: Target categorization of aerosol and clouds by continuous multiwavelength-polarization lidar measurements. *Atmos. Meas. Tech.*, **10**, 3175–3201, https://doi.org/10.5194/amt-10-3175-2017.

——, and Coauthors, 2021: Californian wildfire smoke over Europe: A first example of the aerosol observing capabilities of Aeolus compared to ground-based lidar. *Geophys. Res. Lett.*, **48**, e2020GL092194, https://doi.org/10.1029/2020GL092194.

Baidar, S., N. Kille, I. Ortega, R. Sinreich, D. Thomson, J. Hannigan, and R. Volkamer, 2016: Development of a digital mobile solar tracker. *Atmos. Meas. Tech.*, **9**, 963–972, https://doi.org/10.5194/amt-9-963-2016.

Bela, M. M., and Coauthors, 2022: Quantifying carbon monoxide emissions on the scale of large wildfires. *Geophys. Res. Lett.*, **49**, e2021GL095831, https://doi.org/10.1029/2021GL095831.

Cai, Y., J. R. Snider, and P. Wechsler, 2013: Calibration of the passive cavity aerosol spectrometer probe for airborne

determination of the size distribution. *Atmos. Meas. Tech.*, **6**, 2349–2358, https://doi.org/10.5194/amt-6-2349-2013.

Cattrall, C., J. Reagan, K. Thome, and O. Dubovik, 2005: Variability of aerosol and spectral lidar and backscatter and extinction ratios of key aerosol types derived from selected aerosol robotic network locations. *J. Geophys. Res.*, **110**, D10S11, https://doi.org/10.1029/2004JD005124.

Damoah, R., and Coauthors, 2004: Around the world in 17 days—Hemispheric-scale transport of forest fire smoke from Russia in May 2003. *Atmos. Chem. Phys.*, **4**, 1311–1321, https://doi.org/10.5194/acp-4-1311-2004.

Das, S., and Coauthors, 2017: Biomass burning aerosol transport and vertical distribution over the South African-Atlantic region. *J. Geophys. Res. Atmos.*, **122**, 6391–6415, https://doi.org/10.1002/2016JD026421.

Deng, M., R. Volkamer, Z. Wang, J. Snider, N. Kille, and L. Romero-Alvarez, 2022: Wildfire smoke observations in the western United States from the airborne Wyoming Cloud Lidar during the BB-FLUX project. Part II: Vertical structure and plume injection height. *J. Atmos. Oceanic Technol.*, **39**, 559–572, https://doi.org/10.1175/10.1175/JTECH-D-21-0093.1.

Diner, D. J., and Coauthors, 1998: Multi-angle Imaging SpectroRadiometer (MISR) instrument description and experiment overview. *IEEE Trans. Geosci. Remote Sens.*, **36**, 1072–1087, https://doi.org/10.1109/36.700992.

Ditas, J., and Coauthors, 2018: Strong impact of wildfires on the abundance and aging of black carbon in the lowermost stratosphere. *Proc. Natl. Acad. Sci. USA*, **115**, E11595–E11603, https://doi.org/10.1073/pnas.1806868115.

Duck, T. J., and Coauthors, 2007: Transport of forest fire emissions from Alaska and the Yukon Territory to Nova Scotia during summer 2004. *J. Geophys. Res.*, **112**, D10S44, https://doi.org/10.1029/2006JD007716.

Fernald, F. G., 1984: Analysis of atmospheric lidar observations: Some comments. *Appl. Opt.*, **23**, 652–653, https://doi.org/10.1364/AO.23.000652.

Garofalo, L. A., M. A. Pothier, E. J. Levin, T. Campos, S. Kreidenweis, and D. K. Farmer, 2019: Emission and evolution of submicron organic aerosol in smoke from wildfires in the western United States. *ACS Earth Space Chem.*, **3**, 1237–1247, https://doi.org/10.1021/acsearthspacechem.9b00125.

Gerbig, C., S. Schmitgen, D. Kley, A. Volz-Thomas, K. Dewey, and D. Haaks, 1999: An improved fast-response vacuum-UV resonance fluorescence CO instrument. *J. Geophys. Res.*, **104**, 1699–1704, https://doi.org/10.1029/1998JD100031.

Gonzalez-Alonso, L., M. Val Martin, and R. A. Kahn, 2019: Biomass-burning smoke heights over the Amazon observed from space. *Atmos. Chem. Phys.*, **19**, 1685–1702, https://doi.org/10.5194/acp-19-1685-2019.

Griffin, D., and Coauthors, 2020: The 2018 fire season in North America as seen by TROPOMI: Aerosol layer height intercomparisons and evaluation of model-derived plume heights. *Atmos. Meas. Tech.*, **13**, 1427–1445, https://doi.org/10.5194/amt-13-1427-2020.

Haarig, M., A. Ansmann, H. Baars, C. Jimenez, I. Veselovskii, R. Engelmann, and D. Althausen, 2018: Depolarization and lidar ratios at 355, 532, and 1064 nm and microphysical properties of aged tropospheric and stratospheric Canadian wildfire smoke. *Atmos. Chem. Phys.*, **18**, 11 847–11 861, https://doi.org/10.5194/acp-18-11847-2018.

Hirsch, E., and I. Koren, 2021: Record-breaking aerosol levels explained by smoke injection into the stratosphere. *Science*, **371**, 1269–1274, https://doi.org/10.1126/science.abe1415.

Kille, N., and Coauthors, 2017: The CU mobile Solar Occultation Flux instrument: Structure functions and emission rates of NH_3, NO_2 and C_2H_6. *Atmos. Meas. Tech.*, **10**, 373–392, https://doi.org/10.5194/amt-10-373-2017.

——, and Coauthors, 2020: Quantifying the relationship between CO mass fluxes and satellite fire radiative power from wildfires. *2020 Fall Meeting*, Online, Amer. Geophys. Union, Abstract A176-0018.

Kim, M.-H., and Coauthors, 2018: The CALIPSO version 4 automated aerosol classification and lidar ratio selection algorithm. *Atmos. Meas. Tech.*, **11**, 6107–6135, https://doi.org/10.5194/amt-11-6107-2018.

Knopf, D. A., P. A. Alpert, and B. Wang, 2018: The role of organic aerosol in atmospheric ice nucleation: A review. *ACS Earth Space Chem.*, **2**, 168–202, https://doi.org/10.1021/acsearthspacechem.7b00120.

Moisseeva, N., and R. Stull, 2021: Wildfire smoke-plume rise: A simple energy balance parameterization. *Atmos. Chem. Phys.*, **21**, 1407–1425, https://doi.org/10.5194/acp-21-1407-2021.

Müller, D., I. Mattis, U. Wandinger, A. Ansmann, D. Althausen, and A. Stohl, 2005: Raman lidar observations of aged Siberian and Canadian forest fire smoke in the free troposphere over Germany in 2003: Microphysical particle characterization. *J. Geophys. Res.*, **110**, D17201, https://doi.org/10.1029/2004JD005756.

——, A. Ansmann, I. Mattis, M. Tesche, U. Wandinger, D. Althausen, and G. Pisani, 2007: Aerosol-type-dependent lidar ratios observed with Raman lidar. *J. Geophys. Res.*, **112**, D16202, https://doi.org/10.1029/2006JD008292.

Nisantzi, A., R. E. Mamouri, A. Ansmann, and D. Hadjimitsis, 2014: Injection of mineral dust into the free troposphere during fire events observed with polarization lidar at Limassol, Cyprus. *Atmos. Chem. Phys.*, **14**, 12 155–12 165, https://doi.org/10.5194/acpd-14-17299-2014.

Ohneiser, K., and Coauthors, 2020: Smoke of extreme Australian bushfires observed in the stratosphere over Punta Arenas, Chile, in January 2020: Optical thickness, lidar ratios, and depolarization ratios at 355 and 532 nm. *Atmos. Chem. Phys.*, **20**, 8003–8015, https://doi.org/10.5194/acp-20-8003-2020.

Paugam, R., M. Wooster, S. Freitas, and M. Val Martin, 2016: A review of approaches to estimate wildfire plume injection height within large-scale atmospheric chemical transport models. *Atmos. Chem. Phys.*, **16**, 907–925, https://doi.org/10.5194/acp-16-907-2016.

Peterson, D., E. Hyer, and J. Wang, 2014: Quantifying the potential for high-altitude smoke injection in the North American boreal forest using the standard MODIS fire products and subpixel-based methods. *J. Geophys. Res. Atmos.*, **119**, 3401–3419, https://doi.org/10.1002/2013JD021067.

Reid, J. S., and Coauthors, 2009: Global monitoring and forecasting of biomass-burning smoke: description of and lessons from the Fire Locating and Modeling of Burning Emissions (FLAMBE) program. *IEEE J. Sel. Top. Appl. Earth Obs. Remote Sens.*, **2**, 144–162, https://doi.org/10.1109/JSTARS.2009.2027443.

Sessions, W. R., H. E. Fuelberg, R. A. Kahn, and D. M. Winker, 2011: An investigation of methods for injecting emissions from boreal wildfires using WRF-Chem during ARCTAS. *Atmos. Chem. Phys.*, **11**, 5719–5744, https://doi.org/10.5194/acp-11-5719-2011.

Teakles, A. D., and Coauthors, 2017: Impacts of the July 2012 Siberian fire plume on air quality in the Pacific Northwest.

Atmos. Chem. Phys., **17**, 2593–2611, https://doi.org/10.5194/acp-17-2593-2017.

Trentmann, J., M. O. Andreae, H.-F. Graf, P. V. Hobbs, R. D. Ottmar, and T. Trautmann, 2002: Simulation of a biomass-burning plume: Comparison of model results with observations. *J. Geophys. Res.*, **107**, 4013, https://doi.org/10.1029/2001JD000410.

Twomey, S., 1977: *Atmospheric Aerosols.* Elsevier, 302 pp.

Val Martin, M., J. A. Logan, R. A. Kahn, F.-Y. Leung, D. L. Nelson, and D. J. Diner, 2010: Smoke injection heights from fires in North America: Analysis of 5 years of satellite observations. *Atmos. Chem. Phys.*, **10**, 1491–1510, https://doi.org/10.5194/acp-10-1491-2010.

Voss, K. J., E. J. Welton, P. K. Quinn, J. Johnson, A. M. Thompson, and H. R. Gordon, 2001: Lidar measurements during Aerosols99. *J. Geophys. Res.*, **106**, 20 821–20 831, https://doi.org/10.1029/2001JD900217.

Wagner, R., M. Jähn, and K. Schepanski, 2018: Wildfires as a source of airborne mineral dust—Revisiting a conceptual model using large-eddy simulation (LES). *Atmos. Chem. Phys.*, **18**, 11 863–11 884, https://doi.org/10.5194/acp-18-11863-2018.

Wandinger, U., and Coauthors, 2002: Optical and microphysical characterization of biomass-burning and industrial-pollution aerosols from multiwavelength lidar and aircraft measurements. *J. Geophys. Res.*, **107**, 8125, https://doi.org/10.1029/2000JD000202.

Wang, Z., and K. Sassen, 2001: Cloud type and macrophysical property retrieval using multiple remote sensors. *J. Appl. Meteor.*, **40**, 1665–1682, https://doi.org/10.1175/1520-0450(2001)040<1665:CTAMPR>2.0.CO;2.

——, P. Wechsler, W. Kuestner, J. French, A. Rodi, B. Glover, M. Burkhart, and D. Lukens, 2009: Wyoming Cloud Lidar: Instrument description and applications. *Opt. Express*, **17**, 13 576–13 587, https://doi.org/10.1364/OE.17.013576.

Willeke, K., and B. Y. H. Liu, 1976: Single particle optical counter: Principle and applications. *Fine Particles: Aerosol Generation, Measurement, Sampling, and Analysis*, B. Y. H. Liu, Ed., Academic Press, 698–729.

Winker, D. M., and Coauthors, 2010: The *CALIPSO* mission: A global 3D view of aerosols and clouds. *Bull. Amer. Meteor. Soc.*, **91**, 1211–1230, https://doi.org/10.1175/2010BAMS3009.1.

——, J. L. Tackett, B. J. Getzewich, Z. Liu, M. A. Vaughan, and R. R. Rogers, 2013: The global 3-D distribution of tropospheric aerosols as characterized by CALIOP. *Atmos. Chem. Phys.*, **13**, 3345–3361, https://doi.org/10.5194/acp-13-3345-2013.

Yu, H., M. Chin, D. M. Winker, A. H. Omar, Z. Liu, C. Kittaka, and T. Diehl, 2010: Global view of aerosol vertical distributions from CALIPSO lidar measurements and GOCART simulations: Regional and seasonal variations. *J. Geophys. Res. Atmos.*, **115**, D00H30, https://doi.org/10.1029/2009JD013364.